PERGAMON

International Journal of Heat and Mass Transfer 43 (2000) 555–575

International Journal of HEAT and MASS TRANSFER

www.elsevier.com/locate/ijhmt

The effect of nozzle aspect ratio on stagnation region heat transfer characteristics of elliptic impinging jet

Jungho Lee, Sang-Joon Lee*

Department of Mechanical Engineering, Advanced Fluids Engineering Research Center, Pohang University of Science and Technology, San 31, Hyoja-dong, Pohang 790-784, South Korea

Received 12 October 1998; received in revised form 1 April 1999

Abstract

The local heat transfer characteristics of an elliptic impinging jet on a heated flat plate were experimentally investigated for various nozzle aspect ratios. Five elliptic nozzles of aspect ratio (AR) of 1, 1.5, 2, 3 and 4 having the same equivalent diameter (D_e) were tested at jet Reynolds number of 10,000 to study the effect of nozzle aspect ratio on the local heat transfer enhancement in the stagnation region. The temperature distributions on the heated flat plate were measured using a thermochromic liquid crystal thermometry with a digital image processing system. The flow structure was visualized using a smoke-wire technique to get a better understanding on the impinging elliptic jet. With varying the nozzle-to-plate spacing, the isothermal contours on the heated flat plate showed the axis-crossover in heat transfer due to the self-induced curvature variation of a three-dimensional jet structure. For smaller nozzle-to-plate spacing ($L/D_e < 4$), as the nozzle aspect ratio AR of elliptic jet increases, the heat transfer rate was increased larger than that for the axisymmetric jet ($AR = 1$) in the stagnation region. This was mainly attributed to the engulfing large entrainment and enhanced large-scale mixing of the elliptic jet. The stagnation point Nusselt number was correlated for the nozzle aspect ratio and the nozzle-to-plate spacing as $Nu_o \propto (AR)^{-0.082}(L/D_e)^{-0.077}$.

Keywords: Impinging jet; Elliptic jet; Nozzle agent ratio; Stagnation region

1. Introduction

Impinging jet heat transfer has been well established as an effective technique for heating, cooling, or drying a target surface and has a variety of engineering applications, including the tempering of glass, the drying of film and textile, and the cooling of hot steel plate and gas turbine cascade. Recently, the jet impingement is also used for the cooling of microelectronic components. Many investigations have been carried out to understand the jet impingement heat transfer characteristics through experiments and numerical calculations [1,2]. Martin [1] and Viskanta [2] reviewed the flow structure and heat transfer characteristics of impinging jets. These surveys have dealt with the effects of Reynolds number, nozzle-to-plate spacing, nozzle geometry, freestream turbulence, cross flow, jet inclination, entrainment, etc.

The effect of jet flow control techniques at the nozzle exit on the impinging jet heat transfer rates has received relatively large attention. Gardon and Akfirat [3] investigated the effect of turbulence on the heat transfer augmentation by controlling free stream tur-

* Corresponding author. Tel.: +82-562-279-2169; fax: +82-562-279-3199.

E-mail address: sjlee@postech.ac.kr (S.J. Lee)

0017-9310/00/$ - see front matter
PII: S0017-9310(99)00167-2

Nomenclature

A	area of gold-coated film (heating area)
a	major axis radius of elliptic nozzle
b	minor axis radius of elliptic nozzle
D	internal diameter of long straight pipe
D_e	equivalent diameter of elliptic jets
f	nonuniformity factor of gold coating
h	local heat transfer coefficient, Eq. (1)
I	electric current across the gold-coated film
k	thermal conductivity of air
L	distance between nozzle exit and impingement plate
L/D_e	dimensionless nozzle-to-plate spacing
Nu	local Nusselt number, Eq. (1)
Nu_o	stagnation point Nusselt number
q_c	conduction heat flux
q_r	radiation heat flux
q_v	convection heat flux, Eq. (2)
R_{xc}	location of the axis-crossover in heat transfer
R/D_e	dimensionless radial distance
Re	Reynolds number based on equivalent diameter, UD_e/ν
T_a	ambient temperature
T_{aw}	local adiabatic wall temperature
T_j	jet temperature
T_w	local wall temperature (liquid crystal temperature on heated flat plate)
U	mean velocity at nozzle exit
V	voltage across the gold-coated film
X/D_e	dimensionless radial distance along major axis
Y/D_e	dimensionless radial distance along minor axis
ε	emissivity of liquid crystal coated on the gold-coated film
σ	Stefan–Boltzmann constant
ν	kinematic viscosity of air

bulence at the nozzle exit. Kataoka [4] investigated the role of artificially induced large-scale eddies on the impingement heat transfer. Obot et al. [5] and Popiel and Boguslawski [6] reported that the nozzle exit configuration is the most important factor affecting the heat transfer near the stagnation region.

Thermochromic liquid crystal (TLC) has been widely used as a reliable temperature sensor in the impinging jet heat transfer studies [7–12]. Goldstein and Timmer [8] visualized the heat transfer images on a flat plate for arrays of impinging jets. Baughn and Shimizu [9], Yan et al. [10], Lee et al. [11] and Lee and Lee [12] measured local heat transfer coefficients for a fully developed axisymmetric jet impinging on a flat plate using TLC thermometry. They obtained heat transfer coefficients using the steady-state method and the results were in good agreement with each other. Recently, the advancement of computer and digital image processing technique has improved the accuracy of temperature measurement using liquid crystals. Especially, Lee and Lee [12] investigated the heat transfer characteristics in the stagnation region with better spatial resolution than previous studies. Lytle and Webb [13] measured flow structures and local heat transfer rates at nozzle-to-plate spacings less than one nozzle diameter and found peculiar behaviors not evident at higher spacings.

Most previous studies on the jet impingement have been focused to the two-dimensional plane jet and axisymmetric circular jet. There were a few impingement jet heat transfer studies using non-circular jets. Tam and Norum [14] studied supersonic rectangular impingement jet from the acoustic point of view. Lee et al. [15] investigated the local heat transfer characteristics of an elliptic impingement jet with an orifice nozzle having aspect ratio of 2.14. The effect of nozzle configuration on heat transfer rates of non-circular impinging jet has not been reported in literatures. Elliptic jets have general behaviors of plane jets and axisymmetric jets depending on the nozzle aspect ratio. The exit momentum thickness of an elliptic jet varies around exit perimeter due to non-uniform curvature distribution. The azimuthal curvature variations of elliptic vortical structures cause non-uniform self-induction and hence complex three-dimensional deformation. These deformations substantially change the flow structure, enhance mixing and increase entrainment of ambient fluids. Especially near the nozzle exit, the jet spreading rate along the minor axis plane is much greater than that of major axis plane, the jet cross-section switches its orientation, so called 'axis-switching' occurs at some downstream distance. The number of axis-switching and its location are strongly dependent on the initial condition and the nozzle shape [16–19].

There were several previous studies on the near-field turbulent structure of elliptic free jet. Ho and Gutmark [16] investigated the coherent structure of elliptic jets having a contraction nozzle of aspect ratio $AR = 2$. They observed flow characteristics such as necking, bending and merging of elliptic vortex rings. They also found that the elliptic free jet had a higher entrainment

rate than the axisymmetric circular jet. Quinn [17] also found that the elliptic jet issued from orifice nozzle with $AR = 5$ has a greater entrainment rate than the axisymmetric jet. Hussain and Husain [18] studied the effects of initial conditions and external acoustic excitation on the flow structure of elliptic jet with contoured elliptic nozzles of $AR = 1.5$, 2 and 4. Lee and Baek [19] investigated that the effect of nozzle aspect ratio on the near-field turbulent structure of elliptic jets using a 3D LDV system for the sharp-edged elliptic nozzles with $AR = 1$, 2, 4 and 8 having the same equivalent diameter $D_e = 60$ mm at $Re = 40{,}000$.

The objective of this study is to understand the effect of nozzle aspect ratio on the heat transfer characteristics of an elliptic impinging jet in the stagnation region and to provide benchmark heat transfer data. The sharp-edged elliptic nozzles with aspect ratio of $AR = 1$, 1.5, 2, 3 and 4 having the same equivalent diameter D_e were tested for the nozzle-to-plate spacings of $L/D_e = 2$, 4, 6, 8 and 10 at the jet Reynolds numbers of 10,000. The relatively large nozzle diameter of $D_e = 25$ mm and the liquid crystal technique were employed in this study to achieve better spatial resolution in heat transfer measurements. As the heat transfer rate on the impingement surface has close relationship with the momentum transfer rate of the impingement jet, flow structures of the impinging elliptic jet were qualitatively visualized using smoke-wire technique with synchronizing laser light sheet.

2. Experimental apparatus and method

2.1. Jet flow system

A schematic diagram of the experimental apparatus is shown in Fig. 1. Air supplied from an axial blower passes through honeycomb, heat exchanger, screens and orifice flowmeter before entering a long straight pipe. Heat exchanger was installed to adjust the air temperature so that the jet temperature issuing from the nozzle is maintained within $\pm 0.1^{\circ}C$ of the ambient room temperature. The volume flow rate was measured with an ASME standard orifice flowmeter capable of measuring air flow rate within $\pm 1\%$ of reading. A long straight PVC pipe with internal diameter D of 52.3 mm and a length of 2.5 m ($48D$) was used in this study.

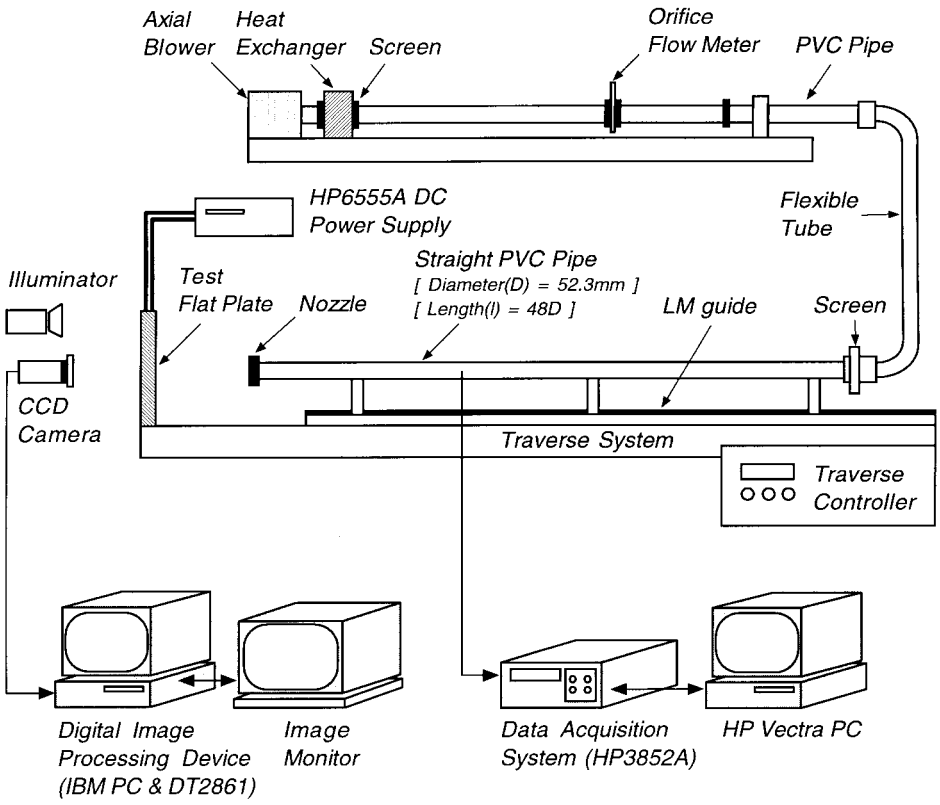

Fig. 1. Schematic diagram of the jet impingement apparatus.

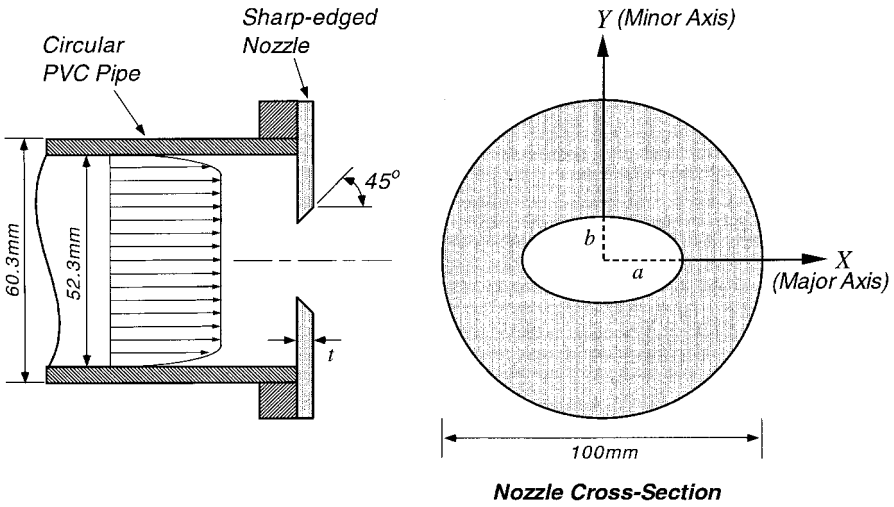

Equivalent diameter of D_e = 25 mm

AR (a/b)	a	b	t
1.0	12.50	12.50	2
1.5	15.31	10.21	
2.0	17.68	8.84	
3.0	21.65	7.22	
4.0	25.00	6.25	

Fig. 2. Configuration of sharp-edged elliptic nozzles (unit: mm).

An elliptic nozzle with sharp-edged type was attached at the downstream end of the pipe, as shown in Fig. 2. This kind of a sharp-edged nozzle has virtually zero momentum thickness in the initial shear layer. Five elliptic nozzles of different aspect ratios $AR = a/b = 1$, 1.5, 2, 3 and 4 were used in this study, where a and b are the major and minor axis radius, respectively. The equivalent diameter D_e is defined as the diameter of an axisymmetric circular jet with a momentum flux equal to that of an elliptic jet, $D_e = 2(ab)^{0.5}$ and is the most appropriate lengthscale for elliptic jets of moderate aspect ratio [18]. All elliptic nozzles used in this study have the same equivalent diameter of 25 mm and are precisely manufactured from brass plate of 2 mm thickness, by a CNC machine. Since the pipe length to the nozzle equivalent diameter was equal to $100D_e$, it ensured the fully developed velocity profile at the nozzle exit. A thermocouple was installed in the pipe 25 mm upstream from the nozzle exit using a feed-through hole to measure the jet temperature. It was a calibrated copper–constantan T type thermocouple of 0.2 mm diameter. The other thermocouple of the same type was placed near the impingement region to measure the ambient temperature. These thermocouples are then connected to HP3852A data acquisition system capable of measuring temperature with an accuracy of 0.08°C. The entire pipe system is rigidly mounted on a traverse device by which the nozzle-to-plate spacing can be adjusted with a resolution of 0.01 mm. During experiments for all elliptic nozzles and nozzle-to-plate spacings, the pressure drop was nearly invariant within ±2%.

2.2. Heated impingement plate

The heated flat plate is composed of Plexiglas flat plate, transparent gold-coated film and thermochromic liquid crystal and its layout is shown in Fig. 3. The impingement plate, 30.3 × 30.3 cm^2, was made of 12.7 mm thick transparent Plexiglas. Plexiglas plate was chosen for its low thermal conductivity which minimizes the heat conduction through the wall. A sheet of gold-coated sputtered film of 17 × 17 cm^2, a thin transparent vacuum-deposited gold-coated film on a 127 μm

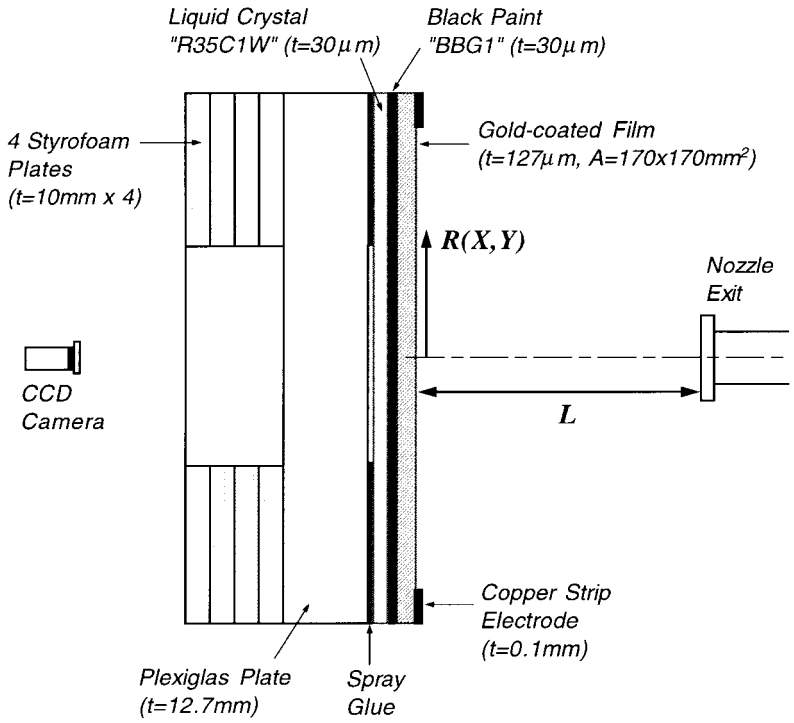

Fig. 3. Layout of impingement test plate and coordinate system.

thick polyester sheet substrate was glued to the upper surface of Plexiglas plate. Two copper-foil strip electrodes were then attached to both end sides of the gold-coated film and silver paint was applied to establish a good electrical contact between the copper electrode and the gold-coated film surface. The copper electrodes are then connected to an accurate DC power supply of HP6555A in series with a current shunt register rated 50 mV and 5 A, allowing adjustable DC voltage to the electrodes. With DC electric current through the heated plate, an essentially uniform wall heat flux boundary condition was ohmically well established on the gold-coated film. HP3852A data acquisition system was used to measure the electric voltage drop across the gold-film and current input to the shunt register. This configuration minimized the uncertainty in the ohmic dissipation measurement less than 1%. To minimize the heat conduction through the wall, four Styrofoam plates of 10 mm thick were placed behind Plexiglas plate. The heat flux on the tested surface was also measured using a heat flux gauge sensor to check the losses owing to thermal radiation and conduction from the impinging plate.

An airbrush was then used to uniformly spray first a layer of black backing paint and then thermochromic liquid crystal on the opposite side of the gold-coated film. The combined thickness of the TLC and black paint was about 60 μm. The liquid crystal used in this experiment was 'R35C1W' microencapsulated TLC purchased from Hallcrest. This TLC has a narrow band of approximately 1°C over which the entire color spectrum occurs (the red color nominally starting at 35.0°C and the blue color starting at 35.8°C).

2.3. Digital image processing system

The image processing system used in this study was consisted of a Panasonic WV-BL600 CCD camera, DT-2861 frame grabber (Data Translation) and IBM PC with an external memory device. The isotherms of red-to-yellow transition band were captured through a red color filter by the CCD camera of 682 × 492 pixels resolution. These captured images were digitized by a frame grabber consisting of 512 × 480 pixels with 256 gray levels and then processed by IBM PC.

The CCD camera captured isothermal contours of the liquid crystal on the heated plate from opposite side of the impinging nozzle. From one-dimensional energy balance across the heated gold-coated film, the temperature difference between the back side of the thin heated film and the impingement surface was found to be less than 0.05°C over the tested experimental conditions. Therefore, the local temperature measured from the back side can be assumed to be identical to that on the impinging surface.

Since the actual color image can be affected from

many factors such as the thickness and surface condition of liquid crystal, the angle of camera and lighting illumination, a careful temperature calibration of liquid crystal was carried out before and after the actual experiments. The TLC and thermocouples with HP3852A data acquisition system were calibrated based on the standard temperature of a platinum resistance thermometer (PRT) with an accuracy of $\pm 0.01^{\circ}$C in a constant temperature bath having a resolution of $\pm 0.01^{\circ}$C. Two lamps located on the same horizontal side of the CCD camera were used to illuminate the color change of liquid crystal on the heated plate. The illuminating angle between the lamps and the impinging jet centerline was set to about 40°.

The liquid crystal was carefully calibrated using the image processing system under the same conditions, including the illuminating light and the CCD camera, as in the actual experiments. The spatial resolution in determining the isotherm locations was estimated to be 0.3 ± 0.05 mm. By selecting spatial locations having the same gray level in the captured image, isothermal contour corresponding to the red-to-yellow transitions can be determined. The TLC calibration results showed that the isotherm for the red-to-yellow color transition on liquid crystal was $34.8 \pm 0.15^{\circ}$C.

2.4. Flow visualization

The smoke-wire flow visualization technique was applied to visualize the near-field flow structure of the elliptic impinging jet. A fine nichrome wire of 150 μm diameter was located horizontally 1 mm in front of the nozzle exit as a smoke-wire. When the electric current was applied to the wire painted with SAFEX fog fluid (Dantec/Invent), small droplets of SAFEX fluid were evaporated to produce white smoke filament lines, i.e., the streaklines. After a fixed time Δt ($\cong 0.07$ s), when the flow pattern was sufficiently traced by the smoke streaklines, a thin laser sheet was produced from a pulsed Nd-YAG laser for 6 ns. Short before the laser firing, the camera (Nikon, F5) shutter was opened with a speed of 1/60 s. To obtain clear photograph with good contrast, the pulsed Nd-YAG laser, camera and a DC power supply for smoke-wire were simultaneously synchronized using a programmable controller.

2.5. Data reduction and uncertainty analysis

The heated gold-coated film provided a nearly uniform wall heat flux boundary condition with thermal conduction and radiation loss to Plexiglas plate on which the gold-coated film was attached. The heat flux was adjusted by changing the electric current through the gold-coated film, which changed the surface temperature. Since the gold-coated film gives constant heat flux condition, an isotherm on the impingement surface corresponds to a contour of constant heat transfer coefficient. As the heat flux input changes, contour of the color isotherm is also changed. The local convective heat transfer coefficient and corresponding Nusselt number at a particular position (red-to-yellow transition) are calculated from

$$h = \frac{q_v}{(T_w - T_j)} \quad \text{and} \quad Nu = \frac{hD_e}{k} \tag{1}$$

where k and T_j are the thermal conductivity of air and the jet exit temperature, respectively. The convective heat flux q_v can be obtained by subtracting the energy losses from the total imposed heat flux input through the gold-coated film and given by

$$q_v = \frac{fIV}{A} - q_r - q_c = \frac{fIV}{A} - \varepsilon\sigma\left(T_w^4 - T_a^4\right) - q_c \tag{2}$$

The conduction heat flux q_c was measured using a heat-flux gauge made of thermopiles. The radial conduction in the heated plate was also calculated by solving the one-dimensional energy equation along the radial direction of plate. The lateral heat conduction in the heated plate was nearly negligible due to styrofoam insulation on the back side of the impingement plate and low thermal conductivity of the polyester substrate. The maximum conduction heat flux q_c was estimated as nearly 3% of the total imposed heat flux. The radiation heat flux q_r was calculated from Stefan–Boltzmann equation and found to be less than 4% of total imposed heat flux. For most experimental conditions, the conduction and radiation losses were 4–7% of the total imposed net heat flux.

In Eq. (2), f is the ratio of the local electric heating to the average heating and accounts for nonuniformity factor of the gold-coated film. Baughn et al. [20] evaluated and found the uniformity to be as high as 97% for a carefully selected gold-coated film, the corresponding size was used in this experiment. We assume $f \approx 1$ for the heat flux calculation, and it contributes to the total Nusselt number uncertainty. The emissivity ε for the liquid crystal coating on gold-coated film was measured by an infrared video camera and found to be 0.9 with an uncertainty of 0.1. The wall temperature T_w was measured using the red-to-yellow color transition of liquid crystal on the impingement heated plate. Since the thermal entrainment of ambient air was minimal due to the fact that the impinging air jet temperature was maintained close to the ambient temperature ($T_a - T_j \leq \pm 0.1^{\circ}$C). In present study, the jet exit temperature was used to calculate the local heat transfer coefficients instead of the local adiabatic wall temperature.

The uncertainty of the local Nusselt number measurements was estimated for all experimental arrangements and procedures using the method

Table 1
Uncertainty of all tested local Nusselt numbers based on 20 to 1 odds method[a]

Individual measurand value x_i	$\lvert\frac{\delta x_i}{Nu}\frac{\partial Nu}{\partial x_i}\rvert \times 100$ (%)
f	2.51–3.94
T_w (°C)	1.53–3.87
V (V)	0.65–2.98
ε	0.61–2.59
I (A)	0.45–2.27
q_c (W/m^2)	0.21–2.11
T_a (°C)	0.49–1.98
T_j (°C)	0.66–1.41
A (m^2)	0.79
D_e (mm)	0.25
k (W/m K)	0.06

[a] Total Nusselt number uncertainty: $\delta N/Nu = 3.21$–4.85 (%).

suggested by Kline and McClintock [21] with 95% confidence level. The estimated total uncertainty in the Nusselt number was ranged from 3.21 to 4.85%. The individual contributions to the total uncertainty are represented in Table 1. The nonuniformity factor of gold coating, f, was the largest contributor to the total uncertainty and its relative uncertainty was about 2.51–3.94%. Another important source of uncertainty was the wall temperature T_w measured by liquid crystal. The electric input voltage V and the emissivity ε were next contributors to total uncertainty. The uncertainties in the Reynolds number and the radial position (R/D_e) along the plate were estimated to be within 2.8 and 0.8%, respectively.

3. Experimental results and discussions

3.1. Flow visualization results

The vortical structures of elliptic jet impinging on a flat plate were visualized using smoke-wire technique and typical results are shown in Figs. 4 and 5. Fig. 4 shows the plane view of an axisymmetric jet ($AR = 1$) for jet Reynolds number of 10,000 at shorter nozzle-to-plate spacing of $L/D_e = 2$. The axial symmetry of the vortex filament can be seen clearly and a mirror reflection is visible at the bottom of the picture. Before impinging the surface, the free jet exhibits the entrainment process with ambient fluids. The initial wave motion due to shear instability is produced at free shear layer and convected downstream, and the large-scale toroidal vortices are developed as shown in Fig. 4.

As the jet approaches to the impingement plate, the vortices are stretched and their sizes grow gradually through rolling-up process. The toroidal vortices reach the impingement plate periodically at a radial position of $R/D_e \cong 0.5$, which approximately corresponds to end-edge of the nozzle tip. After impinging on the plate, the large-scale vortices stretch in the radial direction along the wall surface and interact with the impingement plate. The convected wall eddies induced from interaction between the large-scale toroidal vortices and the impingement surface can be clearly seen in the region ranged as $1.4 \le R/D_e \le 1.6$. The wall eddies are stretched and diverged in the radial direction in some pulsating patterns. With going further on the plate, the toroidal vortices and the induced wall eddies are abruptly merged and the transformed into a turbulent radial wall jet.

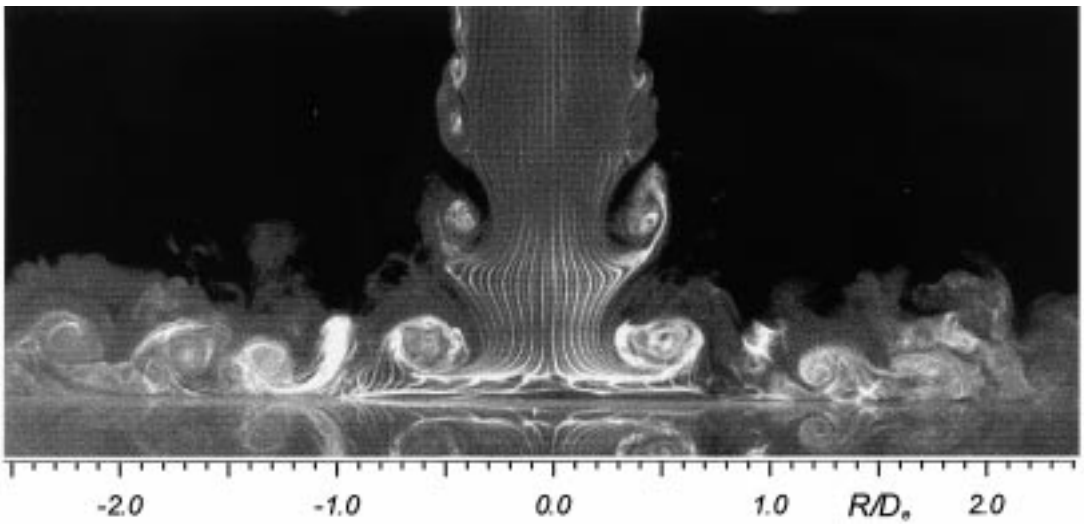

Fig. 4. Flow visualization of axisymmetric impinging jet ($AR = 1$) for $Re = 10{,}000$ and $L/D_e = 2$.

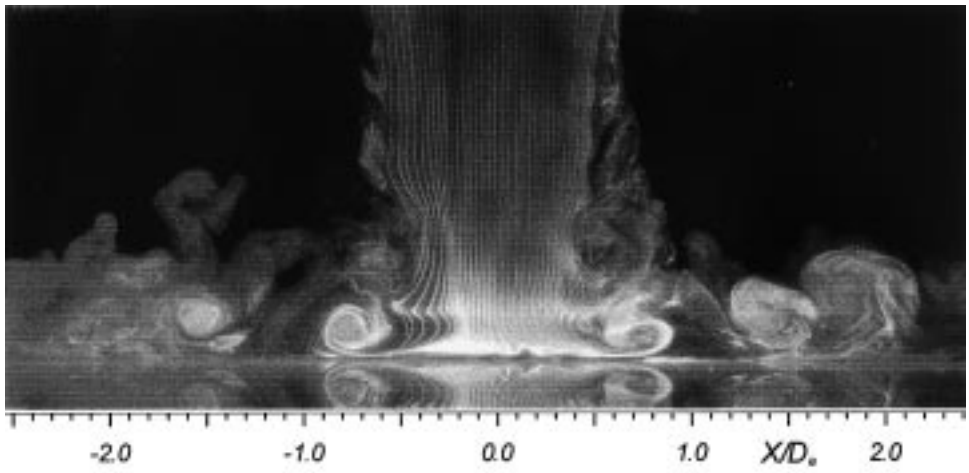

(a) Major axis plane

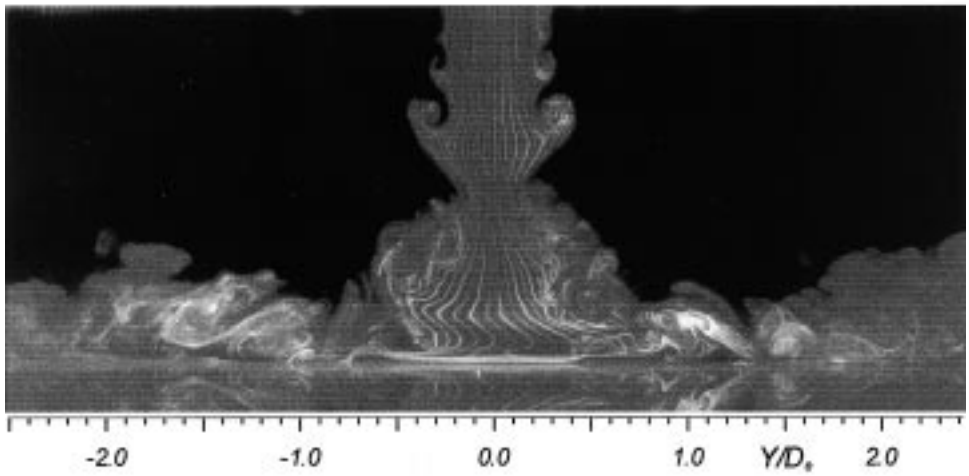

(b) Minor axis plane

Fig. 5. Flow visualization of elliptic impinging jet ($AR = 2$) for $Re = 10{,}000$ and $L/D_e = 2$: (a) major axis plane; (b) minor axis plane.

The general flow pattern of large-scale toroidal vortices and the upstream shear layer vortices are similar with results of Popiel and Trass [22] who visualized the axisymmetric ($AR = 1$) impinging jet issuing from a contoured nozzle. But, the sharp-edge nozzle jet of present study has larger entrainment and strong mixing than that for the contoured nozzle jet [22] due to active rolling-up and earlier paring process at jet shear layer. Beyond about $L/D_e > 4$ the flow in the stagnation region becomes very chaotic and is dominated by the large-scale turbulent fluctuations with the imposed fine-scale turbulence.

The visualized flows for the elliptic impinging jet of $AR = 2$ along the major and minor axis plane are shown in Fig. 5. The smoke-wire was placed across the major axis and minor axis plane of the nozzle exit. The elliptic jet shows quite different flow structures compared with the axisymmetric jet. Since the elliptic nozzle gives azimuthal curvature variation in the initial vortical structure, the elliptic vortical structure is

evolved in different ways along the major and minor axis planes. At the vicinity of stagnation point, the impinging jet exhibits a slight pulsating flow pattern due to deformation of the vortical structure. Along the major axis plane, the large-scale vortical structure start to entrain ambient fluids and the jet width is gradually decreased. The necking of the filament pattern occurs at $1.2D_e$ from the nozzle exit. However, in the minor axis plane, the jet width seems to shrink initially and then to expand largely. Therefore, the major and minor axis of the jet cross-section switch their orientation at some downstream location ($\cong 2D_e$) from the nozzle exit, which is strongly attributed to the self-induction caused by the azimuthal deformation and the interference of the elliptic ring pairs. This axis-switching phenomenon has been also observed in previous studies on elliptic free jets [16–19].

The large-scale toroidal vortices impinge on the flat plate at $0.6 \leq X/D_e \leq 0.8$ on the major axis and $0.35 \leq Y/D_e \leq 0.40$ on the minor axis of the elliptic nozzle of aspect ratio $AR = 2$ for the nozzle-to-plate spacing of $L/D_e = 2$. The induced wall eddies can be also seen in the region of $1.2 \leq X/D_e \leq 1.5$ and $1.5 \leq Y/D_e \leq 1.7$ along the major and minor axis plane, respectively. For aspect ratios larger than 2, not shown in here, the vortices are greatly stretched and the vorticity is substantially increased, and then the vortical structures is rapidly deformed. From Fig. 5, we can see the effect of impingement plate on the flow structure of elliptic free jet. The straight vortex filaments in the jet core region are deflected at about $0.4D_e$ above the flat surface. They are helically twisted due to the self-induced elliptic vortical structures.

3.2. Local heat transfer rate-axisymmetric jet impingement ($AR = 1$)

The local Nusselt number distributions in the stagnation region of axisymmetric jet ($AR = 1$) at jet Reynolds number of 10,000 are represented in Fig. 6. To investigate the effect of nozzle configuration, the local heat transfer rates of the fully developed pipe jet [12] and the contoured jet [3] at the same condition $Re = 10{,}000$ and $L/D_e = 2$ are compared. For present axisymmetric jet issued from a sharp-edged orifice nozzle, the heat transfer contours on the heated plate are nearly circular shape and the local Nusselt numbers were obtained by averaging the values on the major and minor axis.

For the nozzle-to-plate spacing of $L/D_e = 2$, the impinging jet shows complex heat transfer characteristics in stagnation region ($R/D_e < 1$) due to reflection, sudden change of flow direction and interaction between the impinging jet and the heated flat plate. The local heat transfer rate begins to increase from the stagnation point toward local first peak position near $R/D_e \cong 0.5$ and then decreases toward the local minimum at $R/D_e \cong 1.2$. After this point, the local Nusselt number increases and attains the second peak and then decreases monotonically into the wall jet region. The local Nusselt number at the first peak (Nu_{1st}) is approximately 10% higher than the stagnation point value (Nu_o). The local Nusselt number at the secondary peak (Nu_{2nd}) is also approximately 12% less than the stagnation point value (Nu_o). Compared with different nozzle configuration, the stagnation heat transfer rate is about 8 and 25% higher than that of fully developed jet [12] and contoured jet [3] at the same Reynolds number, respectively. The first and secondary peak values are about 11 and 18% higher than those of the fully developed jet. This heat transfer augmentation is mainly attributed to the jet flow structure itself [5,6]. Among these three nozzle configurations, the sharp-edged orifice nozzle of present study was found to be efficient for enhancing the local heat transfer rate.

The first peak in local Nusselt number distributions, corresponding to the maximum heat transfer rate, occurs near the nozzle edge location ($R/D_e \cong 0.5$). This location of the first peak is exactly coincided with the flow visualization result shown in Fig. 4. The large-scale toroidal vortices above the impingement plate mainly result in the local maxima in heat transfer. They lead to a local thinning of the boundary layer with accelerating flow velocity at lower nozzle-to-plate spacing [3]. For a fully developed pipe jet, the turbulent intensity and turbulent kinetic energy have maximum values at the position of $R/D_e = 0.5$ for the nozzle-to-plate spacings less than four nozzle diameters [23].

The secondary peak at $R/D_e \cong 1.5$ also agrees approximately with the location of induced interacting toroidal vortices between the large-scale toroidal vortices and the impingement plate as shown in Fig. 4. Popiel and Trass [22] suggested that the ring-shaped toroidal vortices formed on the impingement surface create a kind of separating boundary between the stagnation region and wall jet region. This secondary peak can also be explained by a transition from laminar to turbulent boundary layer in the developing process towards the spreading wall jet [3,24].

For the case of $L/D_e = 4$, the heat transfer rates do not show remarkable local maximum and minimum values as shown at $L/D_e = 2$. A weak local maximum is observed at $R/D_e \cong 0.2$resulted from remaining effect of the large-scale toroidal vortices. The stagnation Nusselt number of the sharp-edged jet is approximately 17% higher than that of the fully developed pipe jet [12]. Though the nozzle-to-plate spacing of $L/D_e = 4$ is also within the potential core, the secondary peak does not occur clearly, however the tendency is remained with nearly constant Nusselt number dis-

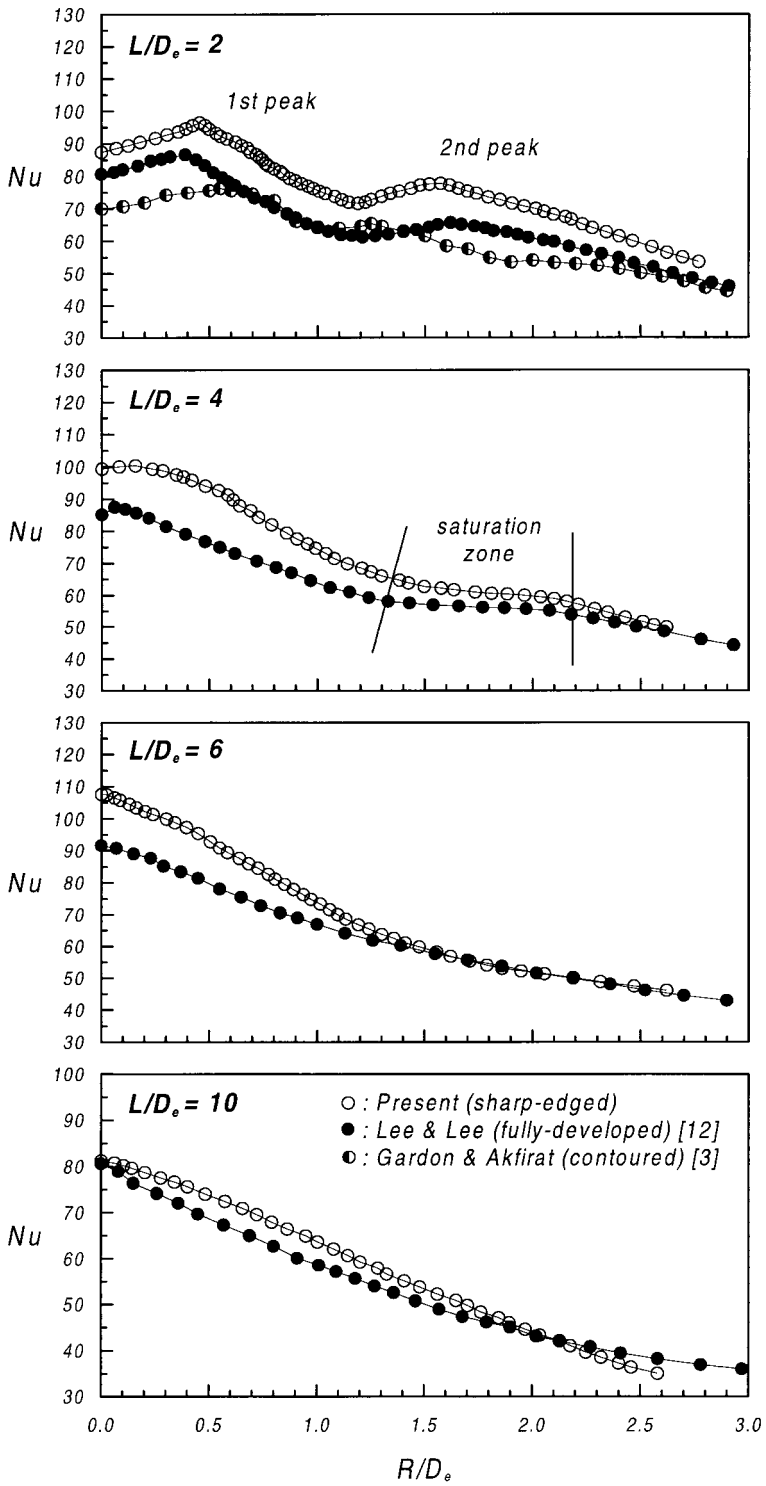

Fig. 6. Local Nusselt numbers for the axisymmetric impinging jet ($AR = 1.0$) at nozzle-to-plate spacings of $L/D_e = 2$, 4, 6 and 10.

tribution in the transition zone between the stagnation region and wall jet region. Thus, we can conjecture that the nozzle-to-plate spacing of $L/D_e = 4$ can be a threshold for the secondary peak to occur. After impinging on the flat surface, the jet undergoes a boundary layer transition towards the wall jet with decaying radial velocity, from which the nearly same amount of heat transfer occurs in the transition region.

For the larger nozzle-to-plate spacing of $L/D_e = 6$ and 10, the local Nusselt numbers decrease monotonically with going outward and do not show the secondary peak at all. The maximum heat transfer rates occur at the stagnation point for $L/D_e = 6$ and 10. The stagnation Nusselt number of the sharp-edged jet is approximately 17% and 10% higher than the fully developed pipe jet [12]. The maximum heat transfer rate occurs at $L/D_e = 6$ due to its highest turbulence intensity. The increase of turbulent intensity leads to heat transfer enhancement at the stagnation point even beyond the potential core length, where the jet centerline velocity is decayed. Many other studies also revealed that the maximum stagnation heat transfer occurs at $L/D_e = 6$ [2,3,6,9–12]. For the nozzle-to-plate spacing of $L/D_e = 10$, the velocity profile becomes self-similar beyond the location of $8D_e$ from the nozzle exit. Moreover, the ambient fluids are entrained up to the jet centerline and the jet loses large amount of momentum before impinging upon the heated flat surface. When the increase in turbulent intensity does not compensate for the decaying jet velocity any more, the heat transfer rate stops to increase. Therefore, the stagnation heat transfer rates for different nozzle configurations are nearly identical at $L/D_e = 10$.

3.3. Local heat transfer rate-effect of nozzle aspect ratio

The effects of nozzle aspect ratio on the local heat transfer rates for the nozzle-to-plate spacing of $L/D_e = 2$ are shown in Fig. 7. In this figure, hollow symbols indicate the local Nusselt numbers along the major axis and solid symbols are for the minor axis. In this case, the impingement plate is within the potential core length of the elliptic jet and the heat transfer characteristics are very complicated due to the complex interactions between the impinging jet and the impingement plate. The local minima in heat transfer occurs at the stagnation point and the moderate first and secondary peak along the major and minor axis are also presented as mentioned in Fig. 6. With the similar trends of an axisymmetric jet, the locations of the first peak along the major axis nearly coincide with end side of the geometrical nozzle exit, respectively.

As the aspect ratio AR increases, the difference in local heat transfer rates along the major and minor axis is increased within the stagnation region. This is attributed to the fact that the spreading rates of elliptic jet of large aspect ratio are significantly different along the two axes. In the stagnation region, the local Nusselt numbers along the major axis is much higher than those along the minor axis, and the major axis of heat transfer contour aligns with that of the nozzle exit. It indicates that the axis-switching of elliptic jet does not occur for the nozzle-to-plate spacing of $L/D_e = 2$ yet. However, the 'axis-crossover' phenomena in heat transfer curves are visible at the transition zone between the stagnation region and the wall jet region for all elliptic jets tested in this study. The 'axis-crossover' in heat transfer is defined as a crossover of local Nusselt numbers along the major and minor axis. This results from the induced vortical interactions between the elliptic vortex rings of jet and the impingement plate [15].

For the elliptic jet of $AR = 1.5$, the local heat transfer rates along the major and the minor axis roughly resemble in general appearance to the case of axisymmetric jet shown in Fig. 6. The first and secondary peak occur at $X/D_e \cong 0.5$ and $X/D_e \cong 1.4$ along the major axis plane, but $Y/D_e \cong 0.4$ and $Y/D_e \cong 1.7$ along the minor axis plane. The axis-crossover in heat transfer rates occurs at $R/D_e \cong 1.6$. In region of $R/D_e > 1.6$, the heat transfer rates along the minor axis become higher than those along the major axis.

For $AR = 2$, the local heat transfer rates along the major axis are higher than those along the minor axis in the stagnation region. The first and secondary peaks are clear and the axis-crossover in heat transfer occurs at $R/D_e \cong 1.75$. The axis-crossover is mainly attributed to difference in the spreading rate along the two axes, i.e. the elliptic jet in the minor axis plane spreads out widely into the ambient fluid, while the shear layer in the major axis plane shrinks toward the jet center. The first peak along the major and minor axis is retained at $X/D_e \cong 0.55$ and $Y/D_e \cong 0.4$. The secondary peak appears near the $X/D_e \cong 1.3$ and $Y/D_e \cong 1.8$ along the major and minor axis, respectively. These peak locations along the major and minor axis show a good agreement with the flow visualization results shown in Fig. 5. The first peak occurs at location of the large-scale toroidal vortices periodically striking the stagnation region and the secondary peak results from the induced vortices formed on the impingement surface between the stagnation region and the wall jet region. These heat transfer results for a sharp-edge elliptic nozzle of $AR = 2$ are agreed approximately with these of elliptic impingement jet using a standard orifice-type nozzle of $AR = 2.14$ [15].

The secondary peak along the major axis does not occur for the elliptic nozzles having aspect ratio of $AR = 3$ and 4, which is attributed to the bifurcation of elliptic vortical structures. The bifurcation phenomena result from the large curvature variation on the major

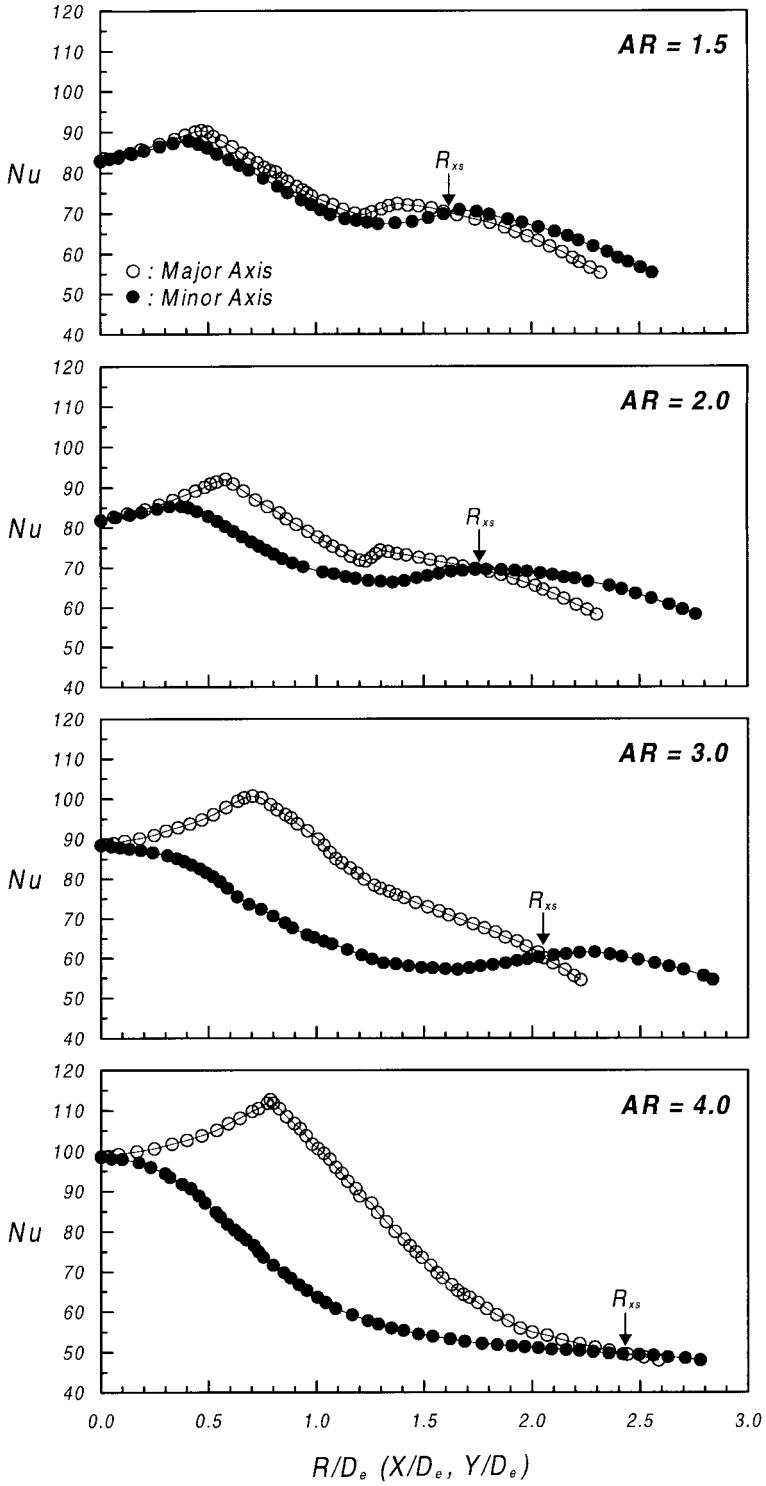

Fig. 7. Local Nusselt number distributions at nozzle-to-plate spacing of $L/D_e = 2$.

axis side [18]. For elliptic jets of $AR = 3$ and 4, the local heat transfer rates along the minor axis have the local maximum value at the stagnation point. The first peak on the minor axis and the secondary peak along the major axis do not occur any more due to the bifurcation phenomena as mentioned above. The axis-crossover in heat transfer occurs at $R/D_e \cong 2.05$ and 2.5 for the aspect ratio of $AR = 3$ and 4, respectively. In addition, the difference in local heat transfer rates between the major and minor planes are larger than the elliptic jets of small aspect ratios ($AR = 1$ and 1.5) due to the deformation and bifurcation of the elliptic vortical structures. In the range of $0.6 < R/D_e < 2.0$, the heat transfer rates along the major axis are much higher than those along the minor axis. The maximum heat transfer at $X/D_e \cong 0.7$–0.8 along the major axis results from the large-scale toroidal vortices on the stagnation region. For the aspect ratio of $AR = 4$, the local Nusselt numbers along the minor axis decrease monotonically.

Comparison results of the local maximum heat transfer rate at the first and secondary peaks for the nozzle-to-plate spacing of $L/D_e = 2$ are shown in Fig. 8(a). They have following relationships for the tested nozzle aspect ratios up to $AR = 4$

$$(Nu_{1st}/Nu_o)_{major} = 1.094AR^{0.033} \quad (3)$$

$$(Nu_{1st}/Nu_o)_{minor} = 1.100AR^{-0.083} \quad (4)$$

$$(Nu_{2nd}/Nu_{1st})_{major} = 0.804AR^{0.001} \quad (5)$$

$$(Nu_{2nd}/Nu_{1st})_{minor} = 0.805AR^{0.014} \quad (6)$$

The ratio Nu_{1st}/Nu_o gradually increases on the major axis as the aspect ratio increases due to the large-scale toroidal vortices and strong mixing with ambient fluid (see Figs. 4 and 5). However, the ratio along the minor axis decreases as the nozzle aspect ratio increases, owing to the difference in spreading rates along the major and minor axis planes as mentioned in Fig. 7. The ratio of Nu_{2nd}/Nu_{1st} is nearly constant for all aspect ratios tested in this study. From this, we can see that the first and secondary peaks are nearly independent of the aspect ratio of elliptic jets.

The radial locations of the first and secondary peaks are also shown in Fig. 8(b) for the nozzle-to-plate spacing of $L/D_e = 2$. With increasing the aspect ratio of elliptic jets, the first peak locations along the major axis are found to increase, but those on minor axis are decreased. The secondary peak locations are vice versa. They have following relationships for the nozzle aspect ratios up to $AR = 4$

$$(R/D_e)_{1st,major} = 0.430AR^{0.430} \quad (7)$$

$$(R/D_e)_{1st,minor} = 0.459AR^{-0.266} \quad (8)$$

$$(R/D_e)_{2nd,major} = 1.565AR^{-0.281} \quad (9)$$

$$(R/D_e)_{2nd,minor} = 1.506AR^{0.336} \quad (10)$$

In Eqs. (7) and (8), the radial positions of the first peak depend on $AR^{0.430}$ and $AR^{-0.266}$ along the major and minor axis, respectively. The distance from the stagnation point to the first peak on the major axis side nearly coincides with the end-edge of the nozzle tips, is increased with the nozzle aspect ratio. However, the peak location along the minor axis decreases with increasing the aspect ratio. The radial locations of the secondary peak are correlated as $AR^{-0.281}$ and $AR^{0.336}$ along the major and minor axis, respectively. Contrary to the first peak, the distance to the secondary peak decreases on the major axis with increase in the aspect ratio. These heat transfer characteristics are highly dependent on the intrinsic flow characteristics of elliptic jets, especially on the quite different jet spreading rates along the major and minor axis.

Fig. 9 shows the local Nusselt number distributions for the nozzle-to-plate spacing of $L/D_e = 4$. The potential core of elliptic jets is shorter in length than that of an axisymmetric jet, even shorter than this nozzle-to-plate spacing of $L/D_e = 4$ depending on the nozzle aspect ratio. At the nozzle-to-plate spacing of $L/D_e = 4$, the impingement plate is then located outside the potential core length for most elliptic jets tested in this study. Except the elliptic jet of $AR = 1.5$, the maximum heat transfer rates occur at the stagnation point. The secondary peaks on the major and minor axis planes do not occur for the case of $L/D_e = 4$.

For the nozzle aspect ratio of $AR = 1.5$, the local heat transfer rates have the maximum value at $R/D_e \cong 0.25$, instead of the stagnation point, due to the remaining effect of the first peak as shown at $L/D_e = 2$. Then the heat transfer rates monotonically decrease along the impingement plate and show a similar behavior of an axisymmetric circular jet ($AR = 1$). The differences in the local heat transfer rates in the stagnation region indicate that the elliptic jet switched its own cross sections of elliptic vortical structure before arriving the impinging plate. The axis-crossover in heat transfer occurs at $R/D_e \cong 2.23$.

For the elliptic jet of $AR = 2$, the local maximum heat transfer rate does occur at the stagnation point and the heat transfer rates along two axes are nearly identical, such as the axisymmetric jet. However, the

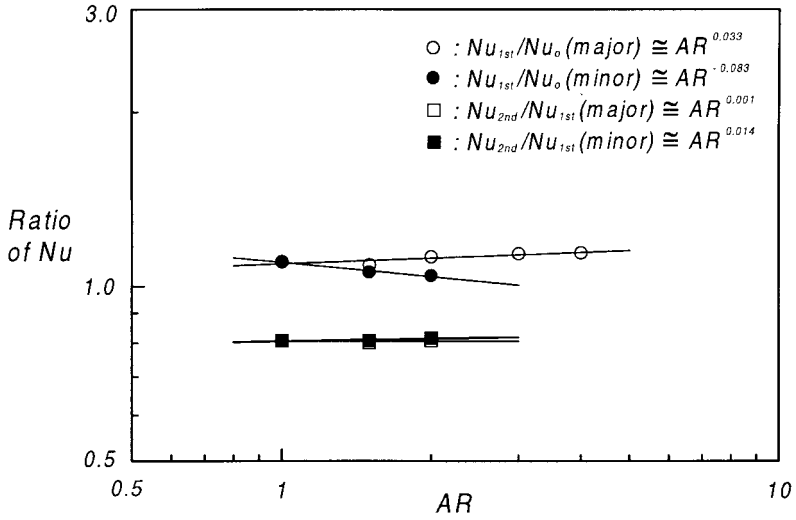

(a) Nu_{1st}/Nu_o and Nu_{2nd}/Nu_{1st}

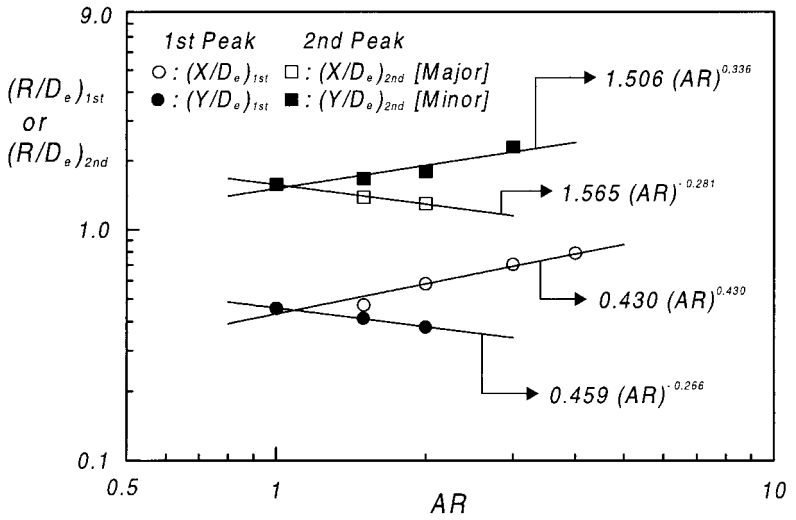

(b) Location of first and secondary peak

Fig. 8. Comparisons of Nusselt numbers at the first and secondary peaks for $L/D_e = 2$: (a) Nu_{1st}/Nu_o and Nu_{2nd}/Nu_{1st}; (b) location of first and secondary peak.

heat transfer rates of elliptic jets are larger in the stagnation region, but smaller in the wall jet region, compared to those of an axisymmetric circular jet ($AR = 1$). This can be explained that the elliptic jet of $AR = 2$ is under the axis-switching process and the nozzle-to-plate spacing of $L/D_e = 4$ is a threshold for the axis-switching. The isothermal contours appeared on the liquid crystal for the elliptic jet of $AR = 2$ show the rhombus pattern of nearly circle shape at $L/D_e = 4$.

The elliptic jets of $AR = 3$ and 4 do not switch their cross section of elliptic vortical structure before arriving the impinging plate. The isothermal contours for the elliptic jet of $AR = 3$ exhibit complicated interactions between the impinging jet and the plate. At the

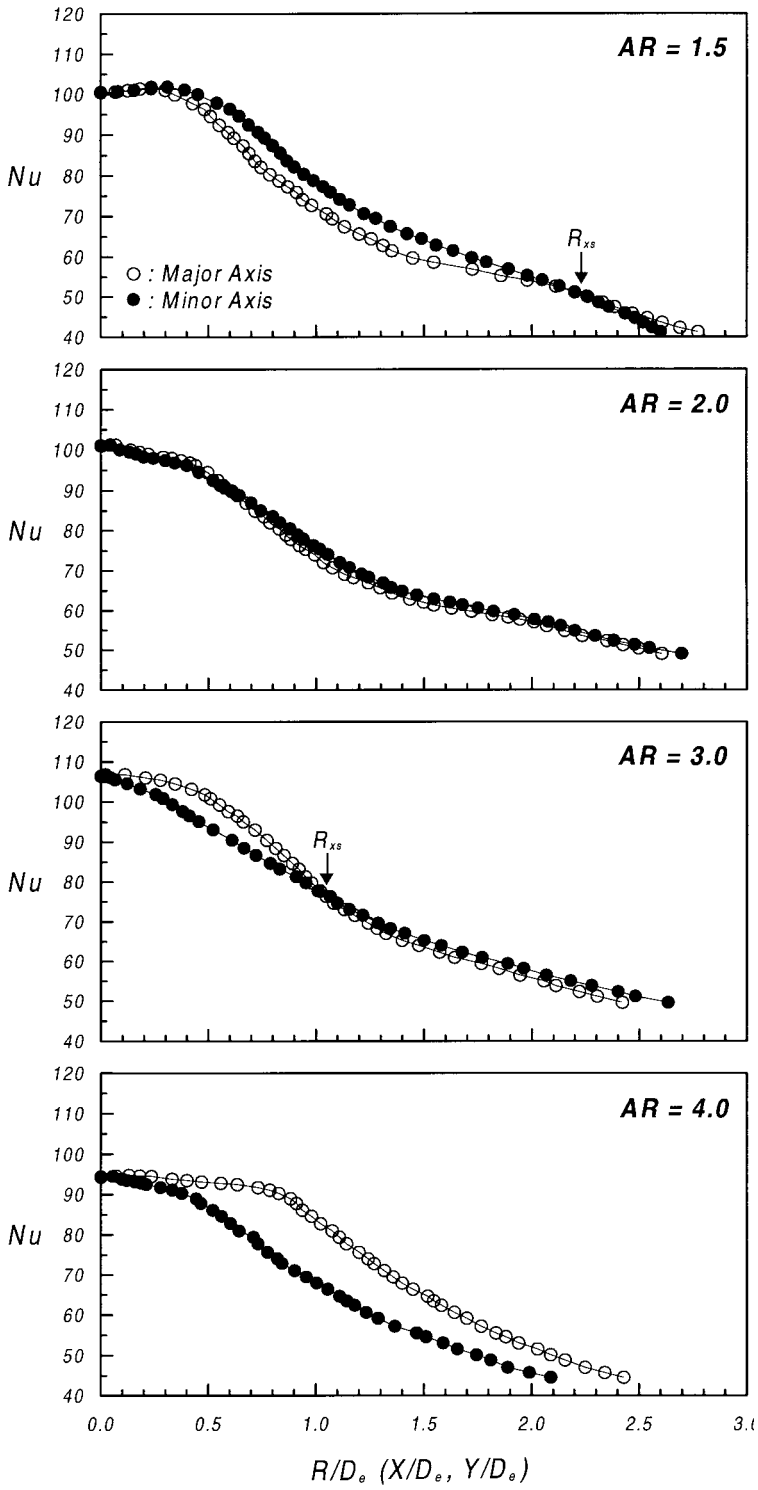

Fig. 9. Local Nusselt number distributions at nozzle-to-plate spacing of $L/D_e = 4$.

stagnation region the same elliptic shape as the nozzle is maintained, with going outward, converted to a rhombus shape at the axis-crossover in heat transfer, and finally to an elliptical shape rotated 90° from its initial nozzle orientation. The axis-crossover in heat transfer occurs near $R/D_e \cong 1.05$, and in the region of $R/D_e > 1.0$, the heat transfer rates along the minor axis are a little higher than those along the major axis. For the case of $AR = 4$, no axis-crossover is seen within the wall jet region of $R/D_e \leq 2.5$. This may be attributed to the bifurcation of elliptic vortical structures and strong convecting flow along the major axis.

Local heat transfer distributions for $L/D_e = 6$ with respect to nozzle aspect ratio are shown in Fig. 10. These profiles show a monotonically decreasing feature of the local heat transfer rates, with going outward along the impingement plate, and do not show clear secondary peak at all. The maximum heat transfer rate occurs at the stagnation point. The axis-switching phenomena in elliptic vortical structures are already appeared for the aspect ratios of $AR = 1.5$, 2 and 3. But, no axis-switching can be still seen for the elliptic jet of $AR = 4$. The heat transfer rates in the wall jet region decrease with approximately same rates, irrespective of the nozzle aspect ratio. The stagnation heat transfer has the maximum value at $AR = 1.5$, smallest nozzle aspect ratio tested in this study. For the axisymmetric impinging jet ($AR = 1$), the maximum stagnation heat transfer is obtained when the impingement plate is placed near $L/D_e = 6$. For $L/D_e > 6$, the increasing turbulence intensity causes the stagnation heat transfer rate to increase even beyond the end of the potential core where the jet centerline velocity start to decay. Previous studies also found that for nozzle-to-plate spacings greater than approximately six nozzle diameters, the maximum heat transfer rate occurs at the stagnation point [3,6,9–12].

For the case of $AR = 1.5$, 2 and 3, the heat transfer rates monotonically decrease along the impingement plate and the axis-crossover in heat transfer is occurred at $R/D_e \cong 2.65$, 2.45 and 2.25, respectively. For the aspect ratio of $AR = 4$, the local maximum heat transfer rate also occur at the stagnation point and the heat transfer rates decrease monotonically along both axes, and the axis-crossover in heat transfer occurs at $R/D_e \cong 2.2$. This indicates that the elliptic jet with $AR = 4$ is still under the axis-switching process of elliptic free jet.

The local heat transfer distributions for the nozzle-to-plate spacing of $L/D_e = 10$ are shown in Fig. 11. The local Nusselt numbers have maximum values at the stagnation point and decrease monotonically with going outward on the impingement plate, and do not show the second maxima at all. For larger nozzle-to-plate distance ($L/D_e > 10$), the velocity profile becomes self-similar and the jet loses vigorous amounts of momentum before impinging upon the flat surface. The heat transfer rates along the minor axis are higher than along the major axis. The difference in local heat transfer rates between two axes increases with going towards the wall jet region. In previous results by Lee et al. [15], the axis-crossover in heat transfer was found at the further locations from the stagnation point, i.e., $R/D_e \geq 3$, this is attributed to the broaden width of elliptic jets having high turbulence fluctuations.

3.4. Stagnation heat transfer and axis-crossover in heat transfer

Fig. 12(a) shows the effect of nozzle aspect ratio on the stagnation heat transfer. For the elliptic jet issuing from the nozzle aspect ratio of $AR = 4$, the stagnation Nusselt numbers are almost linearly decreased. For the case of $AR = 1$ (axisymmetric jet), 1.5 and 2, the maximum stagnation Nusselt number occurs at $L/D_e = 6$. The effect of the nozzle aspect ratio on the heat transfer enhancement is dominant for smaller nozzle-to-plate spacings ($L/D_e = 2$ and 4). This attributes to the strong mixing and large spreading rate of elliptic jets compared with a circular jet, due to the azimuthal curvature variations of an elliptic vortex ring by self-induction of the large-scale coherent structure.

For the nozzle-to-plate spacing of $L/D_e = 2$, the maximum stagnation Nusselt number occurs at the elliptic jet of $AR = 4$. The second order in magnitude is the elliptic jet of $AR = 3$, then $AR = 1$, $AR = 1.5$ and the aspect ratio of $AR = 2$ has the minimum stagnation heat transfer rate. This order in magnitude has a good agreement with the order in streamwise turbulence intensity and kinetic energy along the jet centerline [18,19]. The sequential order in the stagnation heat transfer rate for $L/D_e = 4$ also exactly coincides with the flow results for the same elliptic free jets. For $L/D_e = 2$, the stagnation Nusselt number for the elliptic jet of $AR = 4$ is about 15 and 20% higher than that of the axisymmetric jet of $AR = 1$ and the elliptic jet of $AR = 2$, respectively. For $L/D_e = 4$, the elliptic jet of $AR = 3$ has the maximum heat transfer rate, which is about 8% higher than that of the axisymmetric jet ($AR = 1$). For the larger nozzle-to-plate spacing of $L/D_e \geq 6$, the stagnation heat transfer rate decreases with increasing nozzle aspect ratio, due to the subsequent decrease in centerline jet velocity with increasing aspect ratio. Therefore, the maximum stagnation heat transfer occurs at the axisymmetric jet of $AR = 1$ for $L/D_e \geq 6$.

The variations of the stagnation Nusselt numbers (Nu_o) with respect to the aspect ratios (AR) at jet Reynolds number of 10,000 are shown in Fig. 12(b). For all tested nozzle-to-plate spacings ($L/D_e = 2$, 4, 6, 8 and 10), a least-square curve fitting of following

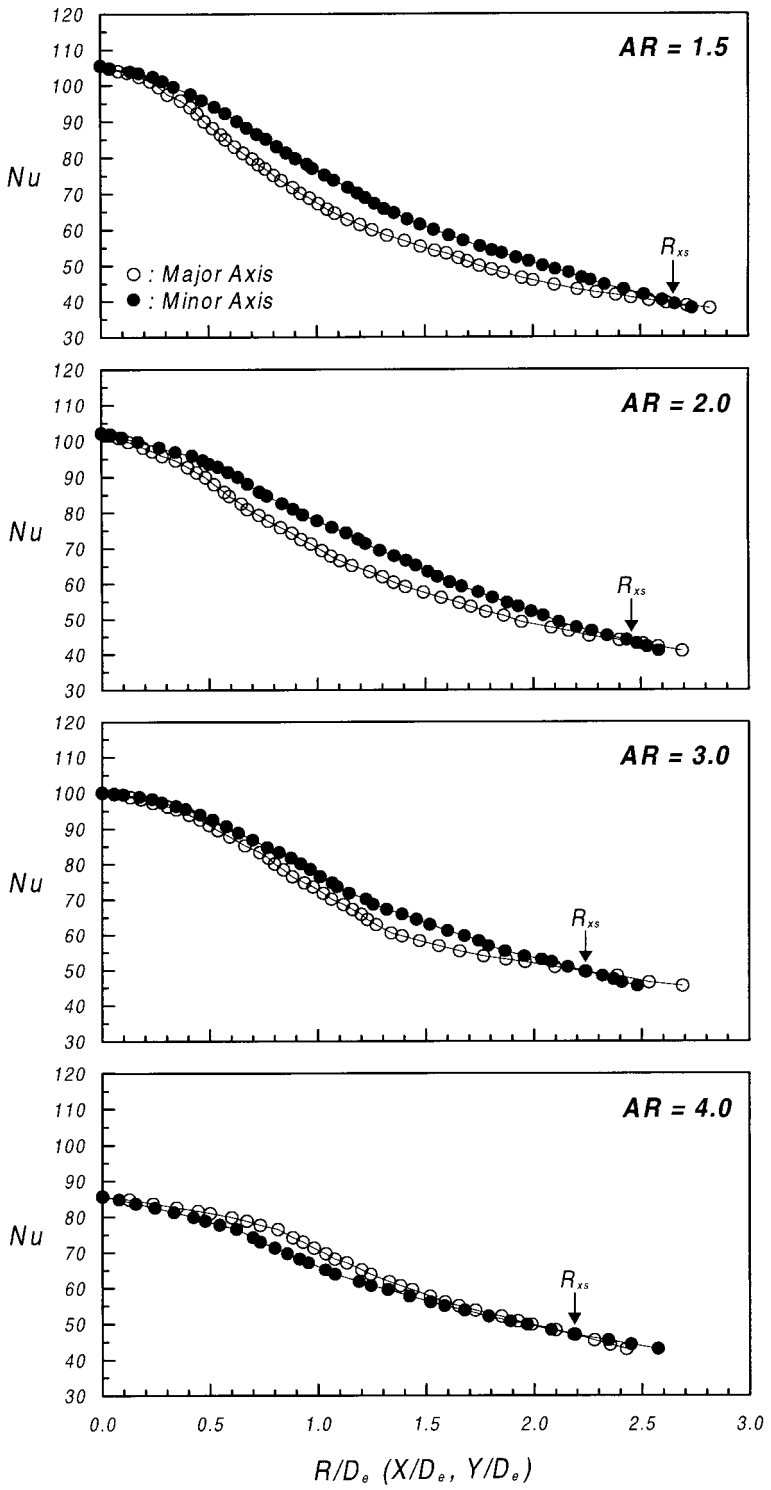

Fig. 10. Local Nusselt number distributions at nozzle-to-plate spacing of $L/D_e = 6$.

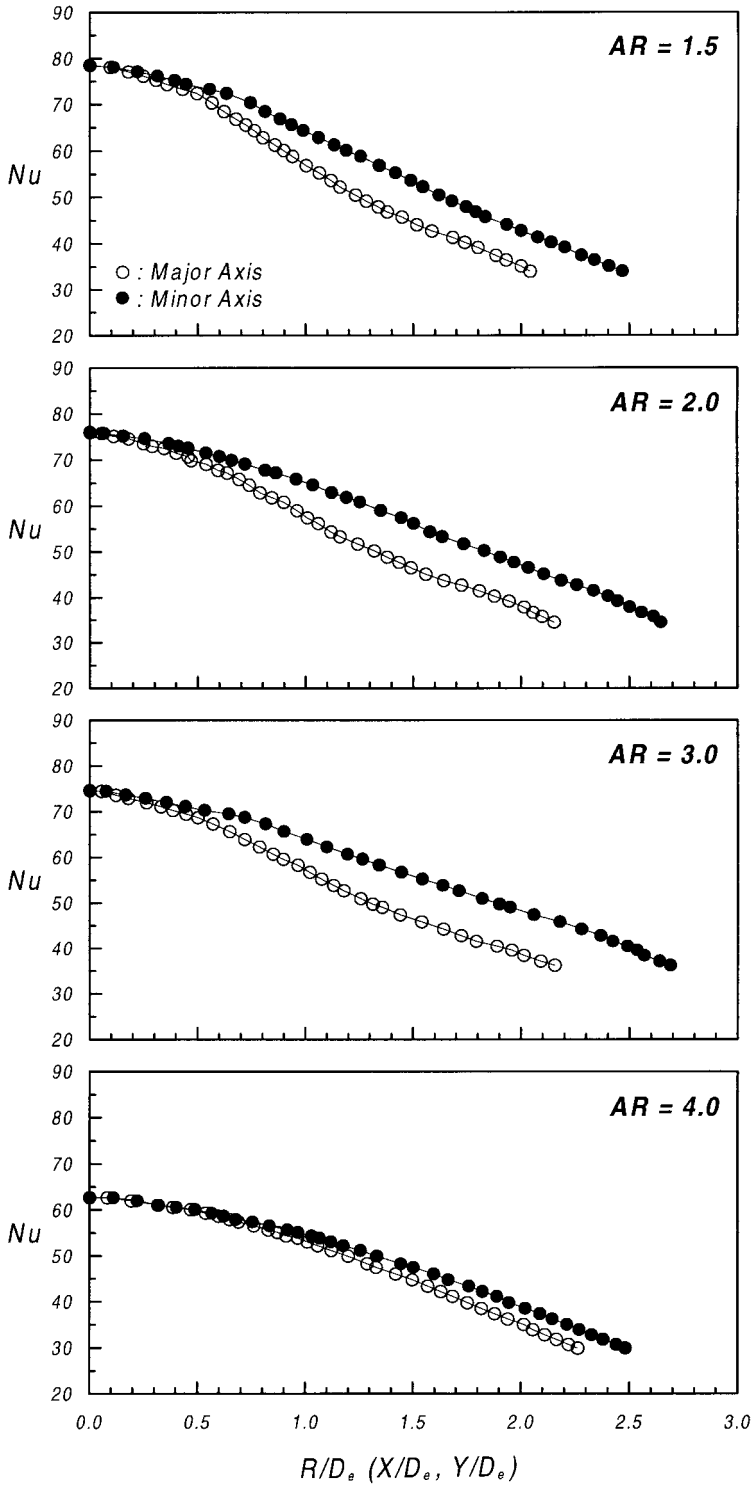

Fig. 11. Local Nusselt number distributions at nozzle-to-plate spacing of $L/D_e = 10$.

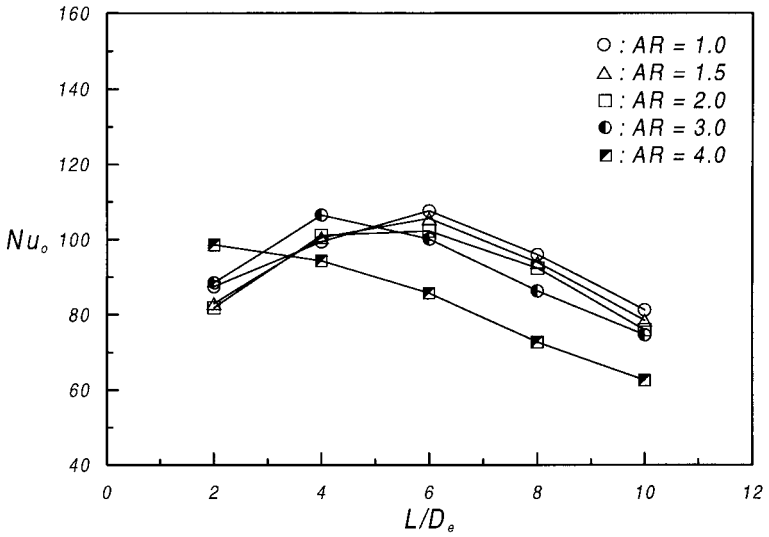

(a) Stagnation Nusselt numbers

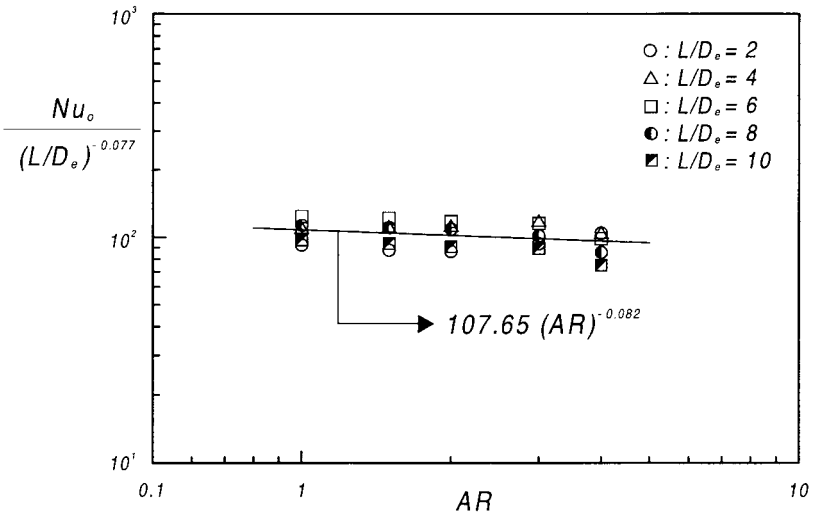

(b) Stagnation Nusselt number correlation

Fig. 12. Variations of stagnation Nusselt number with respect to the nozzle aspect ratio: (a) stagnation Nusselt numbers; (b) stagnation Nusselt number correlation.

form is derived

$$Nu_o = 107.65(AR)^{-0.082}(L/D_e)^{-0.007} \quad (11)$$

This correlation has 5.6% standard derivation error and shows the nozzle aspect ratio dependence on the stagnation Nusselt number of impinging elliptic jets.

Fig. 13 represents locations of the axis-crossover in heat transfer as a function of the nozzle aspect ratio at $L/D_e = 2$ and 6. A least-square correlation for the axis-crossover data can be estimated to have the following form for the tested experimental conditions.

$$R_{xc}/D_e = 1.344(AR)^{0.412} \quad \text{for } L/D_e = 2 \quad (12)$$

$$R_{xc}/D_e = 2.844(AR)^{-0.200} \quad \text{for } L/D_e = 6 \quad (13)$$

The correlations of Eqs. (12) and (13) show 2.6 and

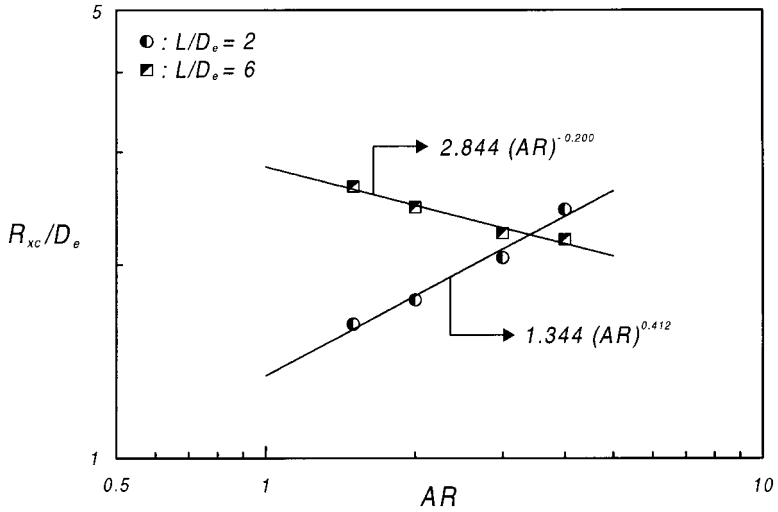

Fig. 13. The axis-crossover in heat transfer for the nozzle-to-plate spacings of $L/D_e = 2$ and 6.

2.1% standard error estimation, respectively. They also reveal the usual dependence of the nozzle aspect ratio on the axis-crossover location in heat transfer for turbulent elliptic impinging jets issued from a sharp-edged nozzle.

For the nozzle-to-plate distance of $L/D_e = 2$, as the nozzle aspect ratio AR increases, the axis-switchover position in heat transfer is increased depending on $AR^{0.412}$. This attributes the large deformations of the elliptic vortical structures on the impingement plate with increasing the aspect ratio as shown in Fig. 7. However, for the larger nozzle-to-plate distance of $L/D_e = 6$, the location of axis-switchover decreases with the aspect ratio of elliptic jets at a rate of $AR^{-0.2}$.

4. Conclusions

The effect of nozzle aspect ratio on the local heat transfer characteristics of elliptic impinging jets on a heated flat plate has been experimentally investigated. Compared with the axisymmetric jet, the curvature dependent self-advection of the elliptical vortical structures produces a three-dimensional deformation, leading to axis-switching and enhanced large-scale mixing. From this, the axis-crossover in heat transfer, which switches its elliptic cross-section of isothermal contours, occurs as peculiar characteristics of elliptic impinging jets. The stagnation Nusselt number was correlated for the aspect ratios and the nozzle-to-plate spacings tested in this study as $Nu_o \propto (AR)^{-0.082}(L/D_e)^{-0.077}$.

For larger nozzle-to-plate distance ($L/D_e > 6$), the heat transfer rates of the elliptic impinging jet are smaller than those for the circular jet in the stagnation region. This is attributed to the fact that center region of the elliptic jet loses large amount of its momentum before arriving the impingement plate due to larger entrainment and stronger mixing with ambient fluid. For the nozzle-to-plate spacing of $L/D_e = 2$, the elliptic jet of $AR = 4$ has the maximum stagnation heat transfer rate, which is about 15% larger than that of the circular jet ($AR = 1$). This results from the high streamwise turbulent intensity and turbulent kinetic energy along the jet centerline due to different spreading rates along the major and minor axis plane. For $L/D_e = 4$, the elliptic jet of $AR = 3$ has the maximum heat transfer rate. Consequently, the elliptic impinging jets can be used as an effective passive control technique for heat transfer enhancement for engineering applications having small nozzle-to-plate spacing less than the potential core length.

Acknowledgements

This study was supported by Advanced Fluids Engineering Research Center (AFERC), POSTECH.

References

[1] H. Martin, Heat and mass transfer between gas jets and solid surfaces, Advances in Heat Transfer 13 (1977) 1–60.
[2] R. Viskanta, Heat transfer to impinging isothermal gas and flame jets, Exp. Thermal Fluid Sci. 6 (1993) 111–134.
[3] R. Gardon, J.C. Akfirat, The role of turbulence in determining the heat transfer characteristics of im-

pinging jets, Int. J. Heat Mass Transfer 8 (1965) 1261–1272.
[4] K. Kataoka, Impingement heat transfer augmentation due to large scale eddies, in: Proceedings of the Ninth International Heat Transfer Conference, vol. 1, Washington DC, 1990, pp. 255–273.
[5] N.T. Obot, A.S. Majumdar, W.J.M. Douglas, The effect of nozzle geometry on impingement heat transfer under a round turbulent jet, ASME Paper No.79-WA/HT-53, ASME, 1979.
[6] C.O. Popiel, L. Boguslawski, Effect of flow structure on the heat or mass transfer on a flat plate in impinging round jet, in: Proceedings of Second UK National Conference on Heat Transfer, vol. 1, University of Strathclyde, 1988, pp. 663–685.
[7] C.J. Hoogendoorn, The effects of turbulence on heat transfer at a stagnation point, Int. J. Heat Mass Transfer 20 (1977) 1333–1338.
[8] R.J. Goldstein, J.F. Timmer, Visualization of heat transfer from arrays of impinging jets, Int. J. Heat Mass Transfer 25 (1982) 1857–1868.
[9] J.W. Baughn, S. Shimizu, Heat transfer measurement from a surface with uniform heat flux and an impinging jet, ASME J. Heat Transfer 111 (1989) 1096–1098.
[10] X. Yan, J.W. Baughn, M. Mesbar, The effect of Reynolds number on the heat transfer distribution from a flat plate to an impinging jet, in: The 1992 ASME Winter Annual Meeting, ASME HTD, vol. 226, Anaheim, 1992, pp. 1–7.
[11] D. Lee, R. Greif, S.J. Lee, J. Lee, Heat transfer from a flat plate to a fully developed axisymmetric impinging jet, ASME J. Heat Transfer 117 (1995) 772–776.
[12] J. Lee, S.J. Lee, Turbulent heat transfer characteristics in a stagnation region of axi-symmetric jet impingement, in: Proceedings of the Eleventh International Heat Transfer Conference, vol. 5, Kyongju, Korea, 1998, pp. 433–438.
[13] D. Lytle, B.W. Webb, Air jet impingement heat transfer at low nozzle-plate spacings, Int. J. Heat Mass Transfer 37 (1994) 1687–1697.
[14] C.K.W. Tam, T.D. Norum, Impingement tones of large aspect ratio subsonic rectangular jets, AIAA J 30 (1992) 304–311.
[15] S.J. Lee, J. Lee, D. Lee, Local heat transfer measurements from an elliptic jet impinging on a flat plate using liquid crystal, Int. J. Heat Mass Transfer 37 (1994) 967–976.
[16] C.M. Ho, E. Gutmark, Vortex induction and mass entrainment in a small-aspect-ratio elliptic jet, J. Fluid Mech. 179 (1987) 383–405.
[17] W.R. Quinn, On mixing in an elliptic turbulent free jet, Phys. Fluids B1 (1989) 1716–1722.
[18] F. Hussain, H.S. Husain, Elliptic jets. Part 1: Characteristics of unexcited and excited jets, J. Fluid Mech. 208 (1989) 257–320.
[19] S.J. Lee, S.J. Baek, The effect of aspect ratio on the near-field turbulent structure of elliptic jets, Flow Meas. Instrum. 5 (1994) 170–180.
[20] J.W. Baughn, P.T. Ireland, T.V. Jones, N. Saniei, A comparison of the transient and heated-coating methods for the measurement of local heat transfer coefficients on a pin fin, ASME J. Heat Transfer 111 (1989) 877–881.
[21] S.J. Kline, F.A. McClintock, Describing uncertainties in single-sample experiments, Mechanical Engineering 75 (1953) 3–8.
[22] C.O. Popiel, O. Trass, Visualization of a free and impinging round jet, Exp. Thermal Fluid Sci. 4 (1991) 253–264.
[23] L. Boguslawski, C.O. Popiel, Flow structure of the free round turbulent jet in the initial region, J. Fluid Mech. 90 (1979) 531–539.
[24] B.N. Pamadi, O.A. Belov, A note on the heat transfer characteristics of a circular impinging jet, Int. J. Heat Mass Transfer 23 (1980) 783–787.